



Weak scratch detection and defect classification methods for a large-aperture optical element

Xian Tao, De Xu, Zheng-Tao Zhang*, Feng Zhang, Xi-Long Liu, Da-Peng Zhang

Research Center of Precision Sensing and Control, Institute of Automation, Chinese Academy of Sciences, Beijing, China

ARTICLE INFO

Keywords:

Optical inspection
Weak scratches
Surface defects classification
Large-aperture optical element

ABSTRACT

Surface defects on optics cause optic failure and heavy loss to the optical system. Therefore, surface defects on optics must be carefully inspected. This paper proposes a coarse-to-fine detection strategy of weak scratches in complicated dark-field images. First, all possible scratches are detected based on bionic vision. Then, each possible scratch is precisely positioned and connected to a complete scratch by the LSD and a priori knowledge. Finally, multiple scratches with various types can be detected in dark-field images. To classify defects and pollutants, a classification method based on GIST features is proposed. This paper uses many real dark-field images as experimental images. The results show that this method can detect multiple types of weak scratches in complex images and that the defects can be correctly distinguished with interference. This method satisfies the real-time and accurate detection requirements of surface defects.

1. Introduction

Large-aperture optics are indispensable in inertial confinement fusion (ICF) high-power laser systems, such as National Ignition Facility (NIF) [1] in the United States and Laser MegaJoule (LMJ) Facility [2] in France, and have the dual function of guiding and amplifying laser beams. The surface defects of large-aperture optics, such as scratches, digs, and bubbles, may harm the safe operation of high-power laser system. Therefore, detecting surface defects has an important practical significance. Currently, automated visual inspection based on the dark-field scattering principle should be a rapid and effective method to detect defects of large-aperture optical elements. There are a number of methods to detect surface defects. The French ICF project LMJ uses a high-resolution 45-Mpixel CCD camera with an LED array edge-illuminating frame [3] to detect defects [4]. proposes a defect detection method using dark-field back illumination and a camera to obtain the flaw information for full sized optics at one time, but the accuracy of these two methods is at most 110 μm [5,6]. design a surface defect evaluation system (SDES) with an area CCD and a precise two-dimensional motion platform. The detection diameter of the SDES is up to 810×460 mm² with a resolution of 0.5 μm , but the image acquisition time in sub-aperture scanning is longer than half an hour. To achieve fast and high-precision detection of large-aperture optical elements, a new and effective inspection instrument [7,8] with two imaging systems for large-aperture optical elements was proposed. It combines a dark-field imaging system (DFIS) with a line-scan

camera at a 10 μm resolution and a bright-field imaging system (BFIS) with a microscopic camera at a 0.85 μm resolution. The DFIS is developed to scan the entire optical element to quickly obtain all of the distributions of surface flaws for coarse detection. BFIS is used to measure the size of the flaws and recognize the flaw type for fine detection.

The original system works well, but defect detection encounters problems in some special conditions. On the one hand, scratches on the optics, such as Nd-doped glass, are usually shallow. In [9] Fig. 1, the depth of the scratch after burnishing is only approximately 200–300 nm, as obtained by an interference microscope. The detected scratches in our previous paper [8] are deep and obvious and can be effectively detected by conventional binarization methods. In some related works [10–12], the detected flaws are also often notably deep or have a large area. However, these detection methods can lead to partial detection and lead to undetectable problems when they encounter these weak scratches. Meanwhile, there are surface defects in the optical element compared to pollutants, such as dust, fibres, dirt, bright spot, fingerprint, and so on. These disturbances are inevitably involved in the inspection and can affect the detection results [13]. realizes automated discrimination between digs and dust particles on optical surfaces using dark-field scattering microscopy. In [14], the machine learning method is applied to classify linear defects and circular flaws. In current detection systems, such as those described in [7,8], these disturbances are removed by manual marking before defect detection begins. This method significantly reduces the detection efficiency. To

* Corresponding author.

E-mail address: zhengtao.zhang@ia.ac.cn (Z.-T. Zhang).

<http://dx.doi.org/10.1016/j.optcom.2016.10.062>

Received 11 July 2016; Received in revised form 26 October 2016; Accepted 28 October 2016

Available online xxxx

0030-4018/ © 2016 Elsevier B.V. All rights reserved.

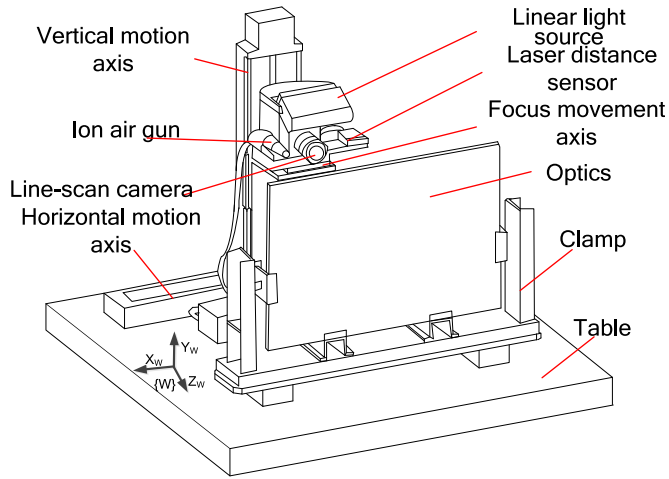


Fig. 1. System layout.

automatically remove pollutants during the detection of surface defects of large-aperture optical elements, there is no relevant report.

Compared with our previous paper [8], this paper focuses more on image processing to solve the two aforementioned problems. In this paper, a coarse-to-fine detection strategy (CFDS) and the defects classification method based on GIST features are proposed. CFDS based on the features of bionic vision and line segment detection (LSD) is proposed, which can detect weak scratches in complicated dark images. First, this method obtains all possible scratches and preliminarily detects the possible scratch segments. Then, for each possible scratch segment, it precisely positions the scratch and connects it to a complete scratch using a priori knowledge. Finally, various types of multiple scratches can be detected in the dark-field image. The defects and interference are classified based on GIST features to improve the detection accuracy. This method is succinct and has a high detecting accuracy and low computational complexity in complex dark-field images. Experiments show that the methods proposed in this paper can quickly and accurately detect various types of weak defects based on dark-field images.

The remainder of this paper is organized as follows. A simple description of the inspection instrument is presented in Section 2. Section 3 provides a detailed illustration of the flaw detection method. A method to distinguish defects and interference is also proposed.

Section 4 shows the experiments and results. Finally, this paper is concluded in Section 5.

2. System setup

The dark-field inspection system for surface defects of large fine optical components is described in detail in Ref. [8]. A brief summary description and supplements are presented here. The inspection system is composed of a clamp unit, a three-dimensional motion unit, a line-scan camera, a laser distance sensor (LDS), an ion air gun and a host computer. The instrument setup is shown in Fig. 1. The clamp unit is used to fix the optical elements to the frame. A line-scan camera is developed to scan the entire optical element to quickly obtain all distributions of surface flaws for detection. The three-dimensional (3-D) movement unit consists of a three-degree-of-freedom (DOF) motion platform with grating rulers. The horizontal axis represents the movement in the X-direction, and the vertical axis represents the movement in the Y-direction. The line-scan camera, ion air gun and LDS are placed on the vertical movement axis. The focusing direction of the line-scan camera represents movement in the Z-direction. The optical axes of the line-scan camera and LDS are parallel to each other. The ion air gun is used to remove dust and fibres on the optical surface because of the electrostatic adsorption effect. The computer is used to control the three-DOF motion platform and capture images. Compared to [8], an additional LDS and ion air gun are included.

In the system, the resolution of the line scan camera is 8192×1 pixels in size and the scanning speed of line scan cameras is 20 mm/s. The maximum size of the optics for inspection is 810 mm \times 460 mm.

3. Defect detection

On the surface of the large-aperture optical element, the depths of most scratches are only a few nanometres. Moreover, there are many types of weak scratches. To clearly image the weak scratches, a strong light is generally used that makes the grey value of the background noise close to or even identical to the grey value of the scratches. Fig. 2(a) shows a dark image of a typical scratch. It contains two random weak scratches on the surface, which are marked in red. Fig. 2(b) shows the dark-field image in 3D. The weak scratches and background have no obvious contrast. The images of the weak scratches after binarization are shown in Fig. 3. The low threshold introduces background noise and uneven illumination areas, which

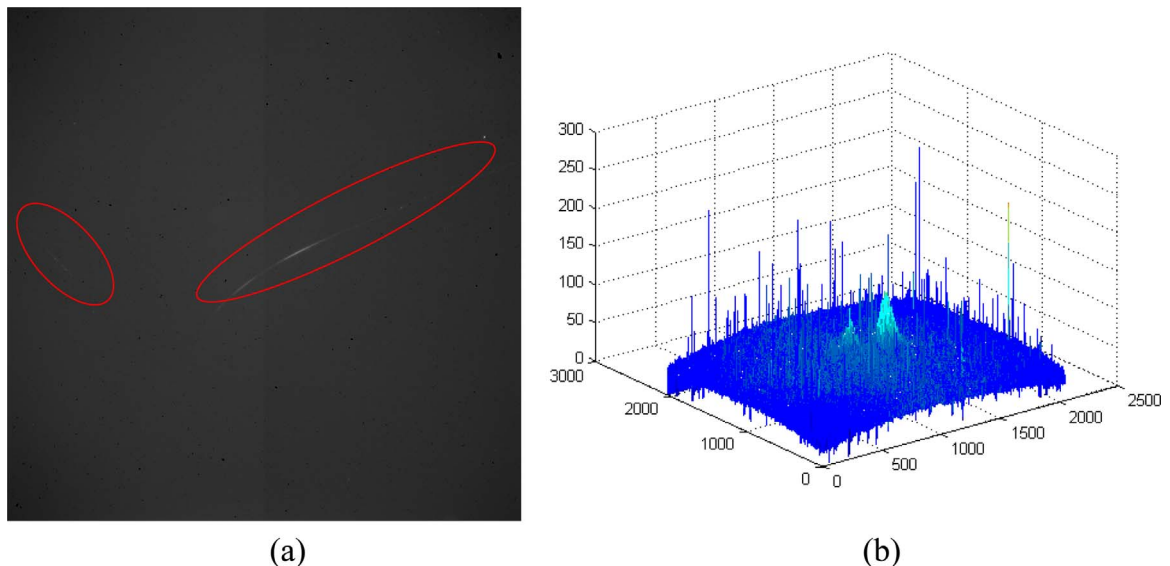


Fig. 2. Images of scratches: (a) a dark-field image captured by the system and (b) a 3D dark-field image. (For interpretation of the references to color in this figure, the reader is referred to the web version of this article.)

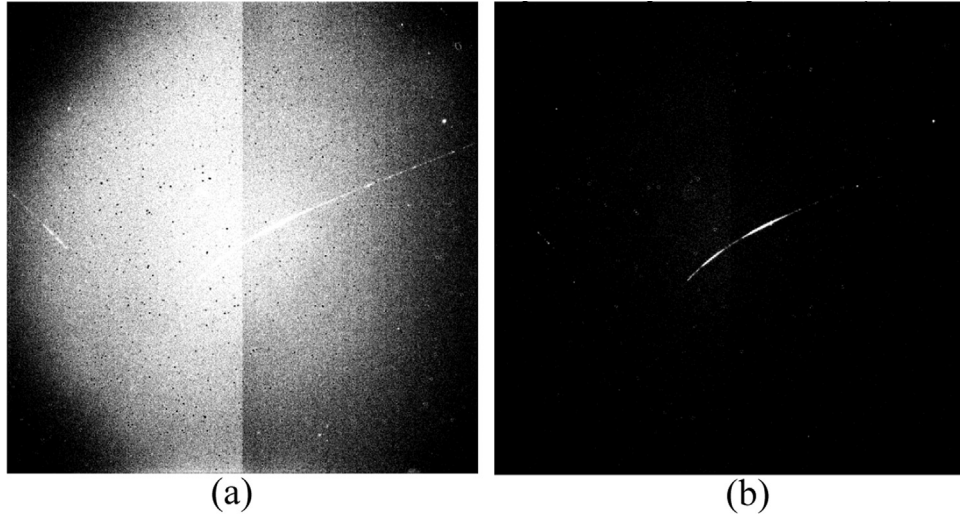


Fig. 3. Processed dark-field image: (a) image processed with a low threshold and (b) image processed with a high threshold.

interfere with feature extraction for scratches. The high threshold classifies the weak scratches as background, which affects the measurement of the total length of the scratch. In the international ISO10110-7 surface defects standard [15], the length of the scratch is an important indicator of the quality of the optics.

3.1. Detection of weak scratch

In general, the main defects in the optical elements are digs and scratches. Fig. 4 shows a dark-field image of digs. Digs are easily exacted in dark-field images because of their high grey values and circular shape. However, the weak scratches are difficult to detect. Although the grey values of weak scratches are close to or even lower than the background values, weak scratches can be easily identified from the background when viewed by the human eye because of the principle of dynamic grouping in the perception of the human visual range. Humans tend to connect elements in different regions that have some commonalities, such as pattern, colour, shape, texture and directionality. Weak scratches are often not continuous, and the edges of scratches have mutated grey values. However, they show a linear arrangement of a series of irregularities in a similar pattern. These patterns can be interpreted as scratch segments to constitute a complete weak scratch.

Therefore, the CFDS of weak-scratch detection is proposed in this paper. The first step is the coarse detection of weak scratches. Using the characteristics of the regional principle in the perception of the human visual range, a coarse-detection algorithm for weak scratches is designed. After coarse detection, all potential scratches can be effectively extracted. Then, a fine-detection algorithm to determine the scratch location and scratch connection is proposed. Finally, using the coarse-to-fine detection strategy, the full information of weak scratches is obtained.

3.1.1. Coarse detection

This process is a binarization of the original dark-field image. In this step, all potential line segments or areas must be extracted, and the

background light noise and uneven illumination areas must be removed using the bionic vision method. When some points have certain grey values along a linear distribution, they may be a potential segment. Based on this principle, four directions (0° , 45° , 90° and 135°) of the line detection units are designed. In Fig. 5(a), the darkest pixel is the point to be binarized (detected). The degree of line detection units is 90° , and the length of the line detection units is W_u , which is 3 in Fig. 5(a). A line detection unit in one direction is divided into three parts: left, middle and right. The sums of the grey values of the left, middle and right parts in Fig. 5(a) are defined as L_l , L_c , and L_r , respectively. In Fig. 5(b), the line direction units in four directions are shown. Straight lines with identical colour and direction are identical line direction units. The rules of coarse detection are defined as follows:

- (1) $I(u, v) > T_1$
- (2) $L_c > L_l + T_2$ and $L_c > L_r + T_2$
- (3) $|L_l - L_r| < T_3$
- (4) $L_l > T_4$ or $L_r > T_4$

As shown in Fig. 5(a), $I(u, v)$ is the grey value of the pixel (u, v) . The direction of potential scratches is the direction of the line detection units when $|L_c - L_l|$ or $|L_c - L_r|$ reaches the maximum value. Rule 1 requires that the point in the potential segments (scratches) cannot be too dark. Rule 2 requires that the point in the potential segments (scratches) of a certain direction is consistent with the line characteristics. A point on the segments should have a higher grey value than one not on the segments. Rule 3 requires that the grey values of the segments on both sides be approximate. This rule removes uneven illumination areas. Rule 4 requires that the segment has a certain width to remove background noise. To increase the detection speed, the current point will be skipped when one of the four rules is not satisfied. T_1 , T_2 , T_3 and T_4 are the thresholds in the four rules. T_1 is obtained based on background sampling in (1). A series of sampled points is obtained, where the sample interval has m rows and n columns in the image space.

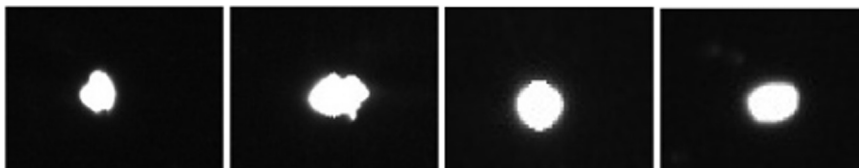


Fig. 4. Dark-field images of digs.

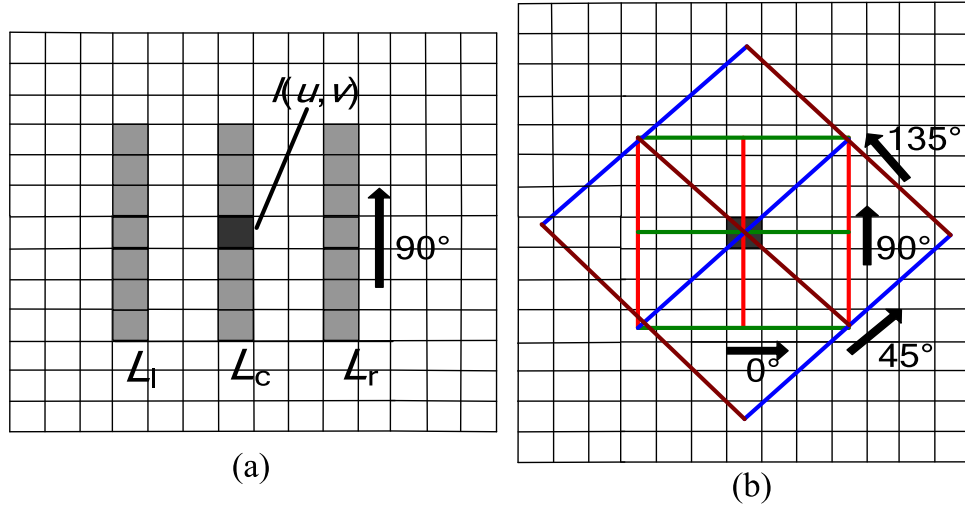


Fig. 5. Sketches of the line detection units: (a) 90° line detection unit and (b) four line detection units. (For interpretation of the references to color in this figure, the reader is referred to the web version of this article.)

$$\begin{cases} T_1 = \frac{1}{n_1 n_2} (\sum_{i=1}^{n_1} \sum_{j=1}^{n_2} I(ni, mj)) + \xi \\ n_1 = \text{Int}(W/n), n_2 = \text{Int}(H/m) \end{cases} \quad (1)$$

where W and H are the image width and height, respectively, and $I(x, y)$ is the grey value of the pixel at the coordinates (x, y) . ξ is an adjustment coefficient. In this paper, we use the following values: $T_1=40$, $T_2=10$, $T_3=40$, $T_4=32$ and $\xi=5$. Fig. 6(a) shows a typical dark image of a scratch with background noise and uneven illumination areas. Weak scratches are marked in red. Fig. 6(b) shows the coarse-detection result. The proposed algorithm can remove the uniform background brightness and high-frequency noise and effectively extract all of the line features in the image.

3.1.2. Fine detection

Scratches in the optical element are formed in the grinding and polishing process. Therefore, they may have various shapes. As shown in Fig. 7, there are seven types of typical scratches on the surface of large-aperture optical elements. (a) Shows a standard single scratch shape with a smaller number, which is easily detected. (b–e) Show the

largest scratch species, which contain line interrupted scratches, point intermittent scratches, point-line interrupted scratches and line-point interrupted scratches. These scratches are initially intermittent or continuous. Because of different depths or uneven thicknesses in the same regions of scratches, the scratches are divided into segments during coarse detection. These segments must be connected into a complete scratch. (f–g) Show two typical interference scratches. (f) Shows two scratches, where there is no dot or segment in the gap. However, the two scratches are consistent in direction, which can be easily connected into an error. (g) Shows a single scratch. There is significant pitting or a dust disturbance near the scratch, so the scratch segments are easily connected to interference. In this step, our goal is to accurately locate and measure these seven types of weak scratches.

The fine-detection algorithm mainly consists of two parts: the region of interest (ROI) location and target linking. The line segment detector (LSD) [16] is applied to locate the line segments in a binary image, as illustrated in Fig. 9(a). The fine-detection method is proposed here.

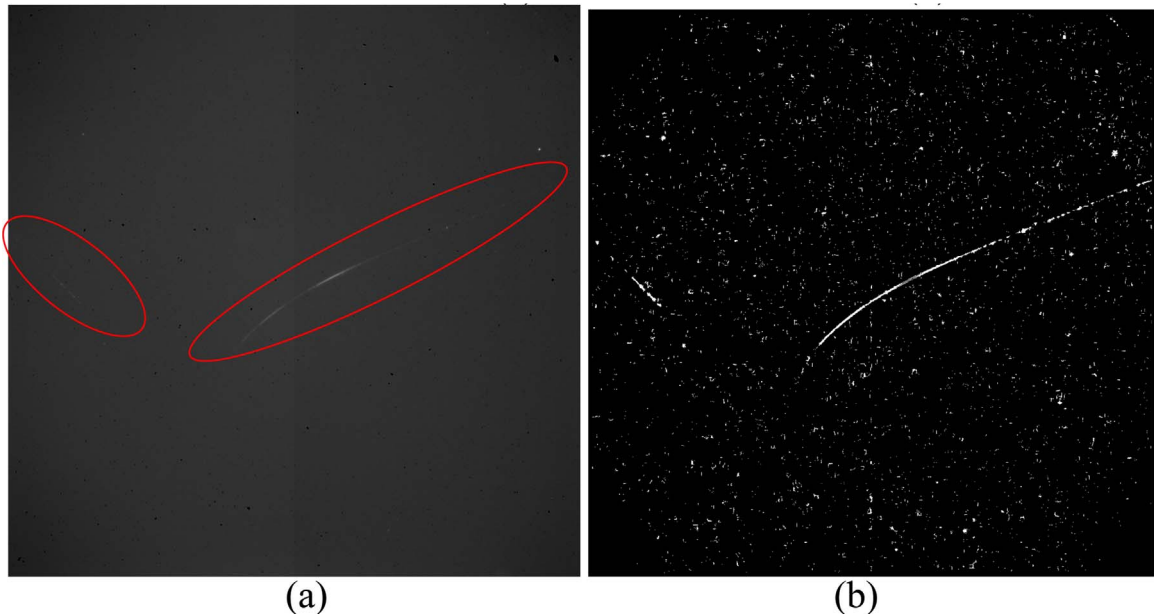


Fig. 6. Dark-field images: (a) the source image and (b) the image after coarse detection. (For interpretation of the references to color in this figure, the reader is referred to the web version of this article.)

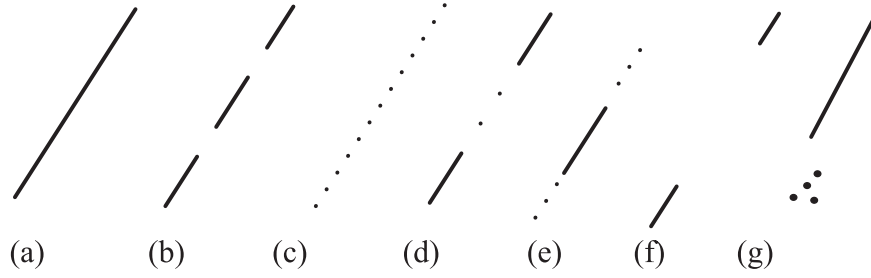


Fig. 7. Scratch types: (a) standard scratch, (b–e) common scratches, and (f–g) scratches with interferences.

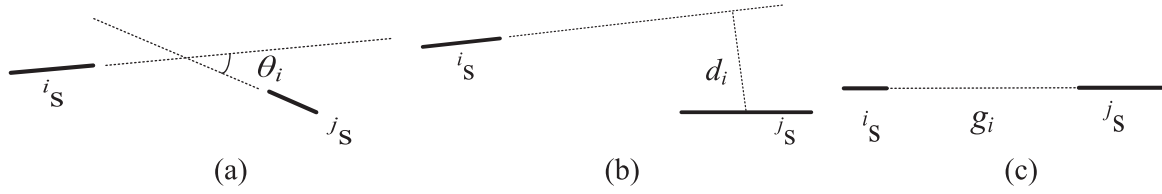


Fig. 8. Schematic view of the rules: (a) intersection angle, (b) distance, and (c) gap..

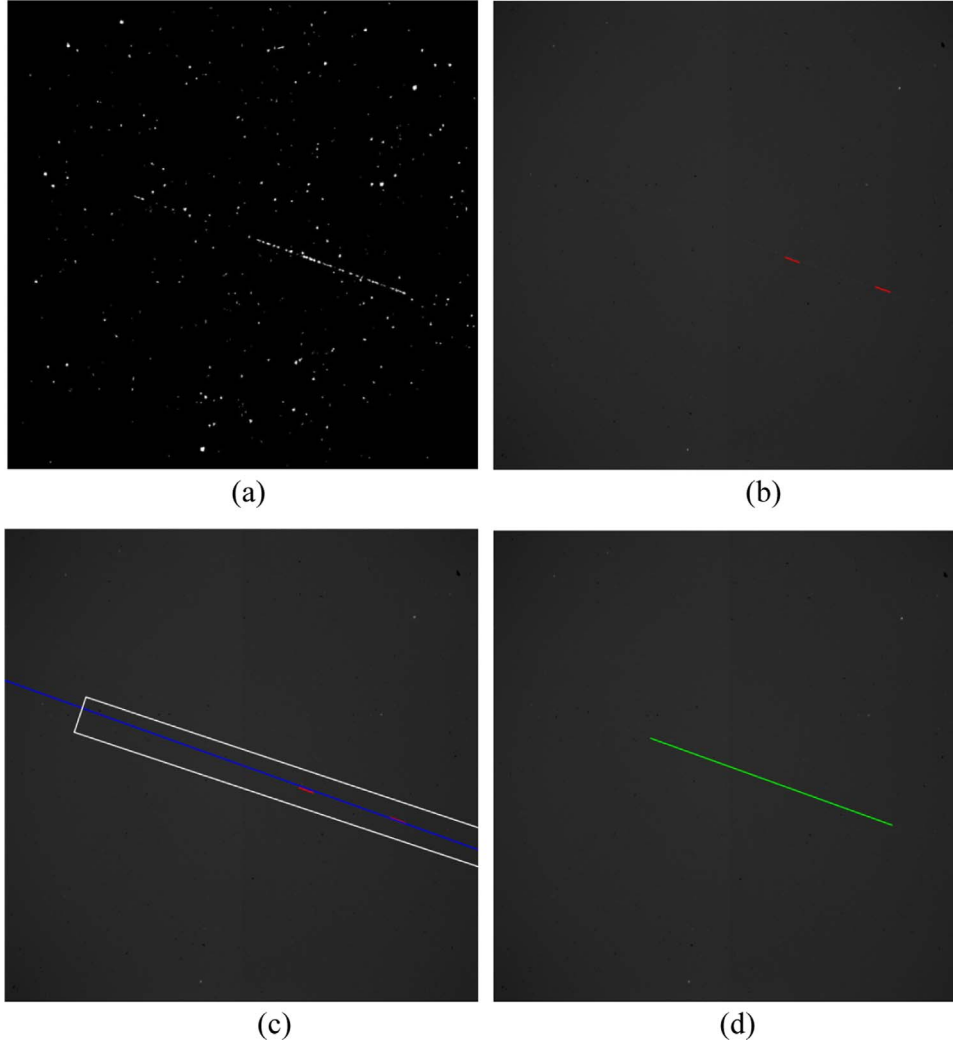


Fig. 9. Fine detection of defects. (a) Image after binarization, (b) LSD result, (c) ROI and the result of RANSAC, and (d) final result. (For interpretation of the references to color in this figure legend, the reader is referred to the web version of this article.)

(1) First, the LSD algorithm is used to precisely locate the potential scratch segments. The result of the LSD, which is labelled in red, is shown in Fig. 9(b). To accurately locate a scratch, a complete scratch detected by the LSD is divided into many small line

segments. Thus, all of the scratch segments after the LSD must be classified as a group. The rules to classify the scratch segments are: intersection angle θ_i between two segments, distance d_i from the midpoint of the segment to another segment, and gap g_i

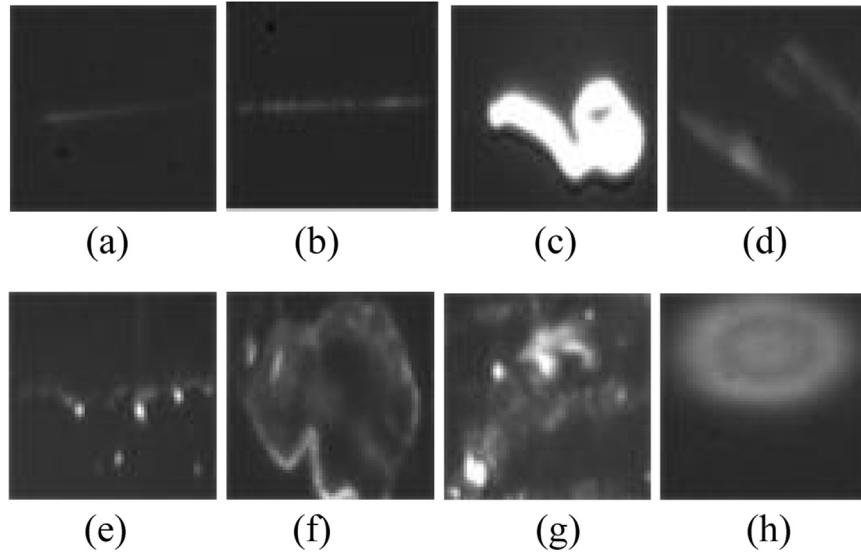


Fig. 10. Dark-field images of defects and pollutants: (a–b) scratches, (c) fibres, (d–e) dust, (f) water stains, (g) fingerprints, and (h) bright spots.

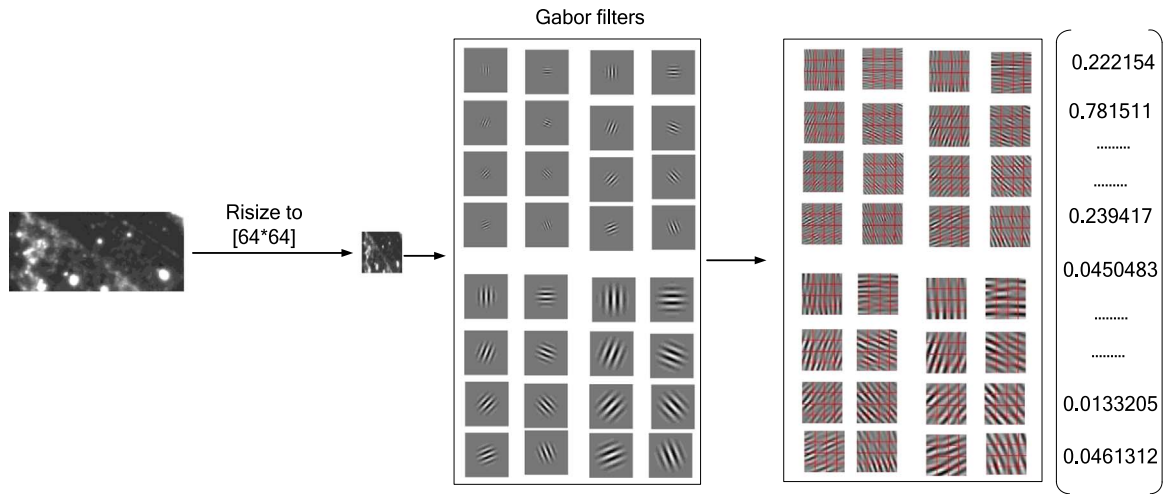


Fig. 11. Extracting the GIST descriptors from dark-field images.

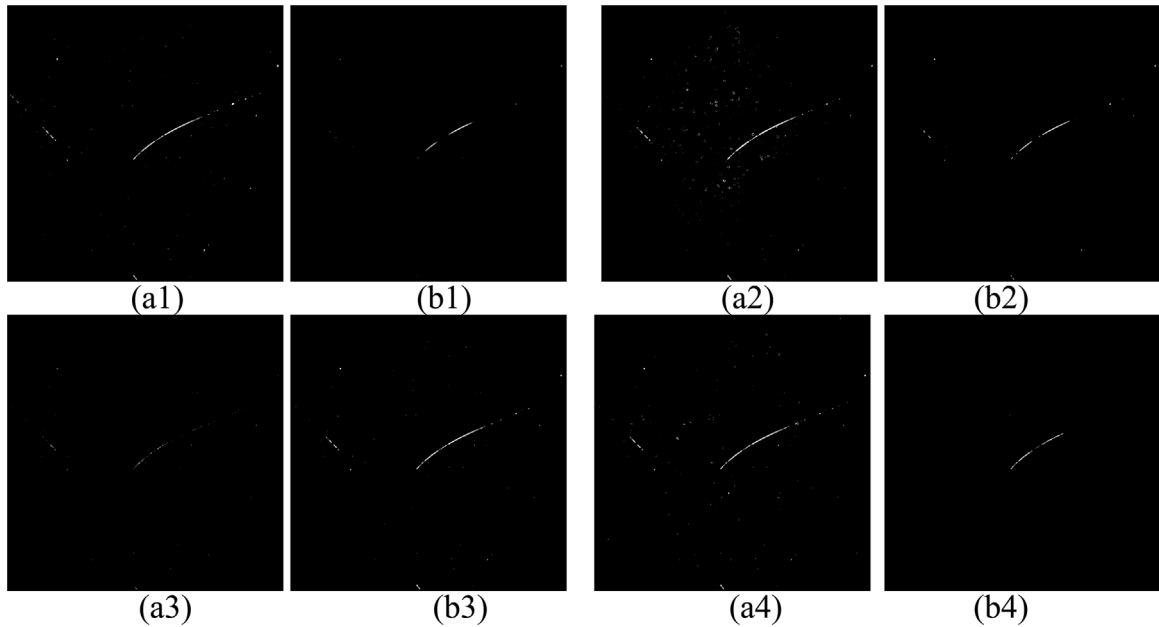


Fig. 12. (a1), (a2), (a3) and (a4) Detection results of decreasing parameters T_1 , T_2 , T_3 and T_4 . (b1), (b2), (b3) and (b4) Detection results of increasing parameters T_1 , T_2 , T_3 and T_4 .

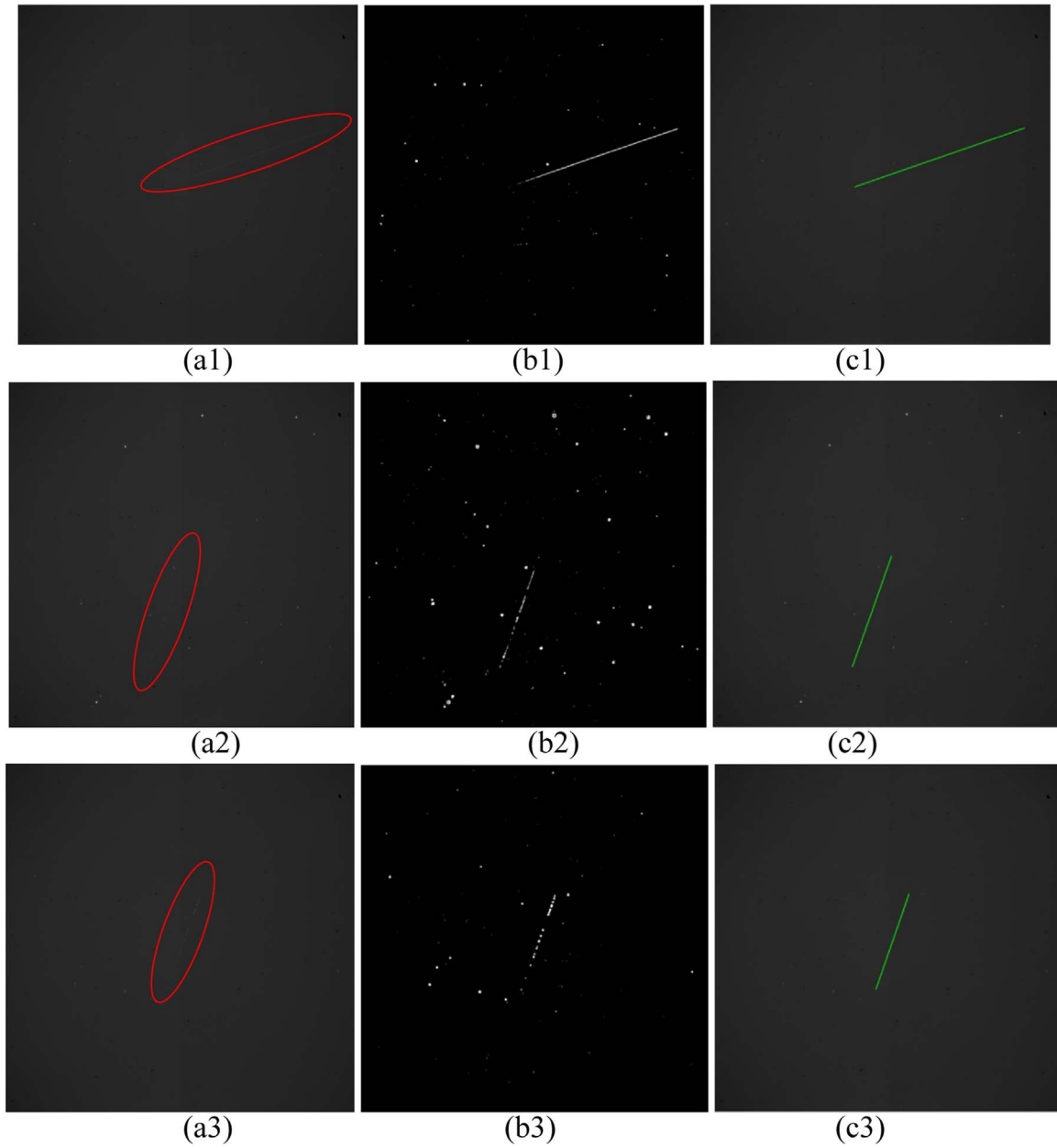


Fig. 13. Detection results of typical scratches: (a1)–(a7) original images; (b1)–(b7) detection result after the coarse detection; (c1)–(c7) detection result after the fine detection. (For interpretation of the references to color in this figure legend, the reader is referred to the web version of this article.)

between two scratch segments. Fig. 8 is a schematic view of the rules. If two segments satisfy these rules, they will be classified as a category. Hence, two segments with identical linear characteristics may come from the same scratch. In this paper, we use the following thresholds: $\theta_i = 12^\circ$; $d_i = 3$ pixels; $g_i = 100$ pixels. The set S of all scratch segments after grouping is

$$S = \{^1s, ^2s, \dots, ^is, \dots, ^ns\}.$$

And

$$^is = \{^i(p_{s1}, p_{e1}), ^i(p_{s2}, p_{e2}), \dots, ^i(p_{sk}, p_{ek})\}.$$

where is is the i -category line segment group, $^i(p_{s1}, p_{e1})$ is the start point and end point of the k -line segment, which is obtained using the LSD.

- (2) All of the points in the ks set are sorted in the direction of its average slope to obtain the start and end points. The length of the scratches can be known from a prior knowledge. We extend the two points based on prior knowledge and obtain an ROI of the rectangular area. The ROI results, which are labelled in white, are shown in Fig. 9(c). In this paper, the extended length along the direction of the line segments is 1000 pixels and the extended length perpendicular to the direction of the line segments is 100 pixels.
- (3) The random sample consensus (RANSAC) algorithm is used in the ROI to obtain an accurate position of the scratch and point set ksr in the scratch. To avoid interference near the scratch, the fitting weights of points can be increased, which are obtained using the LSD. After RANSAC, the points in ksr are returned to the original dark-filed image to calculate the grey values. If the grey value of the points in ksr is too large, it may be dust or dig. These points should be removed in ksr . The result of RANSAC, which is labelled with the blue line, is shown in Fig. 9(c).

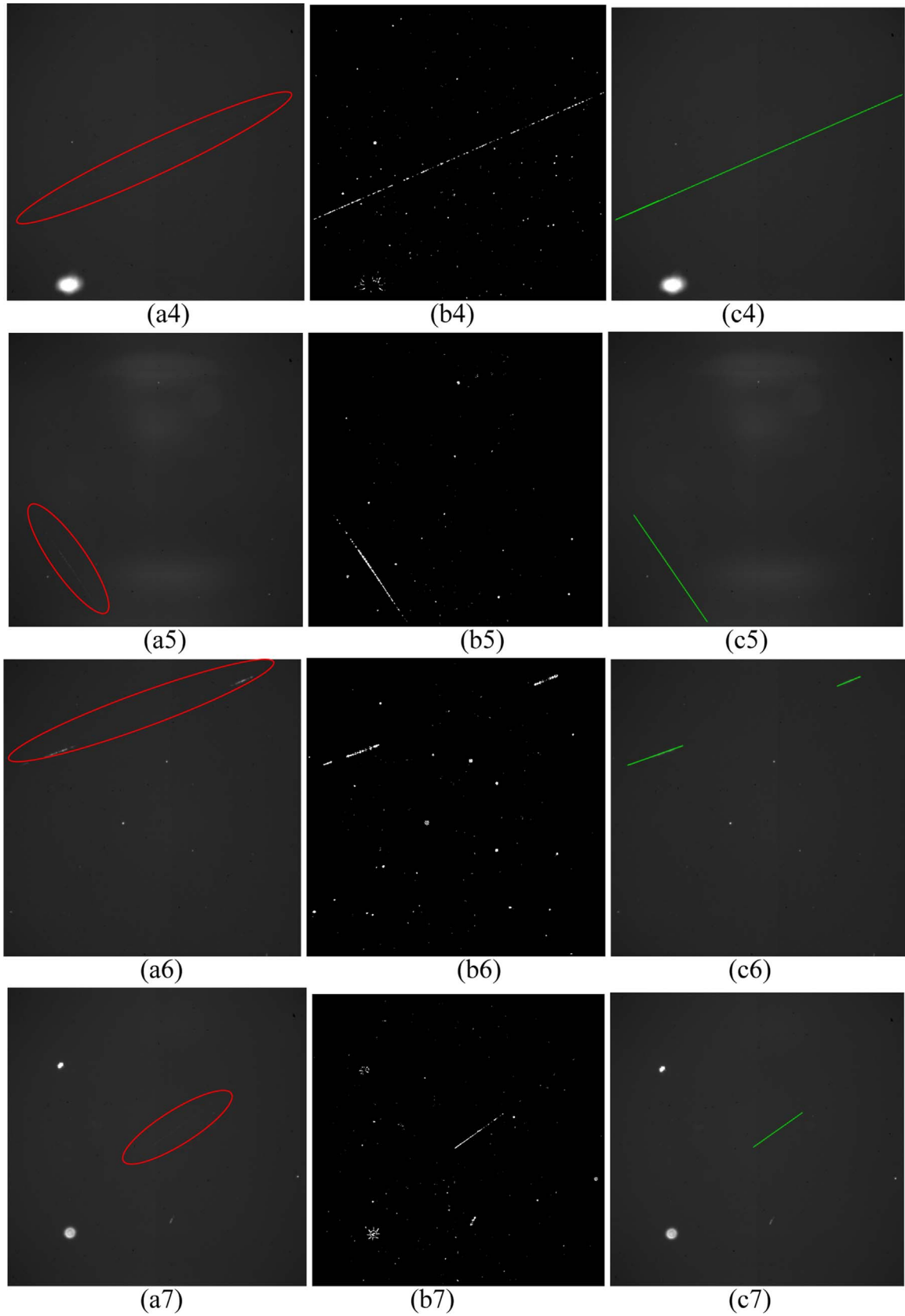


Fig. 13. (continued)

(4) The points in ksr are used to link the scratch segments to a complete scratch using the probabilistic Hough transform [17]. The conditions for linking the line segments are: number of points

on the segment, length of the segment and maximum value of the connected interval (gap) between adjacent segments. These conditions are also the input conditions of the probabilistic Hough

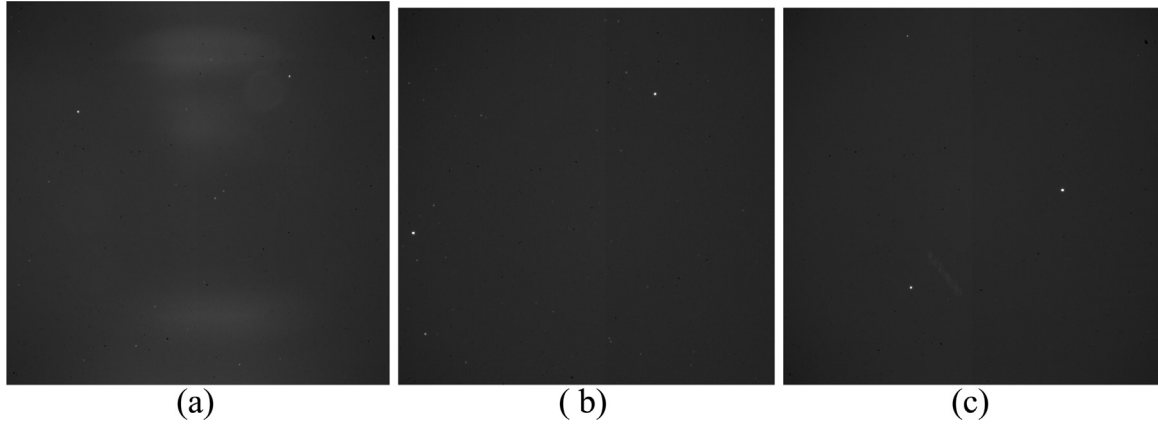


Fig. 14. Detection results of dark-field images with no targets.

Table 1

Comparison of the scratch length using different methods .

Index	N-LSD (mm)	Literature [19] (mm)	Ours (mm)	Manual inspection (mm)	Actual size (mm)
1	182	168	187.8	180	190
2	389	340	410	393	416
3	245	215	255.9	239	252
4	110	104	130.9	116	128
5	41	34	45.1	32	44
6	72	68	74.1	66	76
7	226	220	235.3	233	237

transform. Finally, the complete scratch in the ROI is obtained.

- (5) Repeat steps 2–4 for all scratch segment categories of set S; then, set L of all scratches is obtained. The scratches in set L must be merged in the final result. The final result, which is labelled with the green line, is shown in Fig. 9(d).

In the process of the fine-detection method, three types of line detection methods are combined. The LSD algorithm is more suitable to locate the local straight outline in the image. To obtain an accurate scratch and remove the interference from dig and dust, the fitting method based on RANSAC is used. To connect broken scratches, the high-efficiency method of the probabilistic Hough transform is used.

3.2. Classification of defects and interference

Surface defects in optics are notably few with respect to pollutants, such as fibres, dirt, bright spots, and fingerprints. These pollutants are inevitably involved in the process of producing, cleaning and transporting the optics before inspection, but they must be distinguished from actual defects to improve the detection accuracy. The dark-field images of defects and pollutants after reducing are shown in Fig. 10.

In the detection of a weak scratch, some pollutants, such as dusts and stains, after the coarse detection also have good linear features, so they are easily erroneously detected as scratches. To classify defects and pollutants, GIST descriptors [18] are used to extract the features of dark-field images. In general, the GIST descriptor is commonly used in

scene classification. The GIST descriptor is the global feature descriptor that uses the Gabor filter, which is notably similar to the response to visual stimuli of simple cells in the human visual system.

Fig. 11 shows the computation process of the GIST description. Gabor filter transfer functions with various orientations and spatial resolution are used to filter an image. Then, the image is divided into $n \times n$ grids. The average filter response is obtained from each grid. Finally, all of the averages are connected into a vector as the feature description of the entire image. The Gabor filter transfer functions with various orientations and spatial resolutions are as follows:

$$\begin{cases} G_{\theta_i}^S = C \exp\left(-\frac{(x_{\theta_i}^2 + y_{\theta_i}^2)}{2\sigma^2(s-1)}\right) \exp(2\pi j(u_0 x_{\theta_i} + v_0 y_{\theta_i})) \\ x_{\theta_i} = x \cos \theta_i + y \sin \theta_i, y_{\theta_i} = -x \sin \theta_i + y \cos \theta_i \end{cases} \quad (2)$$

where C is a positive constant; (u_0, v_0) is the time-domain frequency of the plane sine wave; σ is the standard deviation of Gauss function; s is the number of scales; θ_i is the orientation of the scale s ; $\theta_i = \pi(i-1)/\theta_s$, $i=1,2,\dots,\theta_s$; and θ_s is the number of filter direction.

In this paper, the GIST descriptor is applied to classify the defects and interference. The region to detect is the ROI in Section 3.1.2. All images are re-scaled to a square image of 64×64 pixels. Then, the region is divided into 4×4 grids, and the number of orientations θ_s and scales is 8 and 4, respectively. Thus, the final Gist descriptor has $4 \times 4 \times 8 \times 4 = 512$ feature dimensions. When the 512 dimensional features are obtained, they are entered into the support vector machine (SVM) classifier to classify them.

4. Experiments

4.1. Scratch detection experiment

The detection performance of the proposed method was tested on several images that were captured in different Nd-doped glasses. The aforementioned threshold parameters T_1 , T_2 , T_3 , T_4 and ξ were determined using many Nd-doped glass detection experiments. The experiment results of changing parameters T_1 , T_2 , T_3 , T_4 are shown in Fig. 12. The dark-field image of Fig. 6(a) was used as an example. Fig. 12(a1), (a2), (a3) and (a4) show the detection result after

Table 2

Classification result of scratches and pollutants.

Method	Number of true positive		Number of false positive		Accuracy
	Scratches	Pollutants	Scratches	Pollutants	
Our method	79	91	1	9	94.44%
GOCM [20]	49	92	31	8	78.33%
GLCM [20]	45	86	35	14	72.78%

decreasing parameters T_1 , T_2 , T_3 and T_4 , respectively. Fig. 12(b1), (b2), (b3) and (b4) show the detection results after increasing parameters T_1 , T_2 , T_3 and T_4 , respectively. The four sets of coarse-detection results in Fig. 12 show that the changing parameters T_1 , T_2 , T_3 and T_4 affect the overall defect information, linear characteristic information, width of the weak scratches and length of the weak scratches, respectively. When T_1 or T_2 decreases, the length of weak scratches increases. However, the length of the scratches can reduce when T_1 , T_2 or T_4 decrease. By adjusting the parameters, weak scratches can be completely extracted under suitable values. When detecting other optical elements, those parameters must be adjusted according to the experiments rules.

In the scratch detection experiment, there are seven different scratches in our test images. Each scratch belongs to a typical flaw in Fig. 7. In addition, there is a large difference among these test images, such as background, interference and structural features. The test image has a size of 2048×2048 pixels and displays a broad variance of each scratch type because they are captured in different optics, positions and environments. The examples in Fig. 13 show the results of the scratches, which are labelled in green lines on the original images. Fig. 13(a1)–(a7) show the original images, where the scratches are marked in red. Fig. 13 (b1)–(b7) show the coarse-detection result. Fig. 13(c1)–(c7) show the fine-detection result. As observed, the proposed algorithm successfully located weak scratches from the dark-field images and obtained the true length of the scratches. In addition, other images with no scratches were tested. As shown in Fig. 14, there are some false targets, such as uneven illumination in the background and light noise, which have a similar structural feature with the scratch. Although no targets were found, the result in Fig. 14 proves that the proposed method has a strong ability to exclude noise and interference. In this experiment, the detection accuracy rate of a weak scratch is 98% for 600 test images.

To prove that the CFDS positively affects weak scratch detection, a method not based on line segment detection (N-LSD) was used as a comparison. The method in [19] was also used as a comparison to evaluate the proposed method. All of the methods extracted weak scratches and measured the total length of the scratches in the optics, but the strategies were different. In N-LSD, the coarse-detection algorithm is also used to extract all potential scratches. Then, the probabilistic Hough transform is directly used to extract the line segment and connect to a complete scratch. In [19], the dual-threshold detection method is applied to extract scratch defects. According to the frequency characteristics of weak scratches, background contrast and spatial characteristics, the algorithm of frequency domain filtering with background difference is used. The overall lengths of the completed weak scratches in the optics of the three different methods are listed in Table 1. With manual inspection, the observed scratches on the optics are manually measured by inspectors under strong light. Because a small scratch was missed in the manual inspection, the scratch length of the manual inspection was used as a reference. The actual size was obtained by multiplying the pixel equivalent to the pixel lengths of the scratches, which were manually measured in the dark-field images.

According to Table 1, the proposed method has a smaller measurement error of the length of the weak scratch. The N-LSD algorithm is similar to our approach, so they have similar detection lengths. However, when some scratches are extremely weak, the N-LSD algorithm fails to connect small scratches [19]. used the frequency method. The limitations of the frequency range lead to many weak scratches being missed, which results in a larger measurement error. Overall, the proposed method is effective for weak-scratch detection.

4.2. Defect classification experiment

In total, 585 samples were selected as training samples, which included 190 scratches and 395 pollutants; 180 samples were selected as test samples, which consisted of 80 scratches and 100 pollutants.

The sample used for detection was the ROI in Section 3.1.2. To facilitate normalization, the obliquely ROI should be rotated to the horizontal. All images were re-scaled to a square image of 64×64 pixels for feature extraction. The number of orientations θ_s and scales s in Eq. (2) was 8 and 4, respectively. Then, to improve the classification speed, the 512-dimensional features used principal components analysis (PCA) to reduce to a particular dimension whose contribution rate was more than 95%. Those features were entered into the SVM classifier to classify the defects and pollutants. The kernel function of the SVM classifier is a linear kernel function. If the classifying result is interference, the fine extraction in steps 3–4 in Section 3.1.2 is not necessary. This process improves the efficiency and accuracy of defect detection.

A comparative experiment was conducted. The comparative method was shown in [20]. There were two texture feature extraction methods that were used to classify surface defects in extruded aluminium profiles, which contain gradient-only co-occurrence matrices (GOCM) and grey-level co-occurrence matrices (GLCM). Features such as the contrast, homogeneity, energy and correlation are derived from co-occurrence matrices for classification. The classifier was also the SVM. The results are listed in Table 2. Our method has a significantly higher recognition accuracy than the method in [20]. Because the scratches were similar to the linear pollutants in the local features, the proposed classification using global features in the dark-field image is more appropriate to identify surface flaws and pollutants.

5. Conclusion

This paper presents a coarse-to-fine detection strategy (CFDS) and defect classification method in dark-field images for defect detection. The CFDS preliminarily detects possible scratch segments based on bionic vision features, which makes full use of the scratch a priori knowledge to exactly link the segments to an entire scratch in the dark-field image. Then, the classification of defects and interference is completed using the SVM based on GIST features. This paper uses many real dark-field images as experimental images. The results show that the proposed method has a high detection accuracy for surface defects of a large-aperture optical element.

Acknowledgements

This work was supported by the National Natural Science Foundation of China under Grants 61227804, 61303177, 61473293 and 61673383.

Appendix A. Supplementary material

Supplementary data associated with this article can be found in the online version at <http://dx.doi.org/10.1016/j.optcom.2016.10.062>.

References

- [1] S.C. Burkhart, E. Bliss, P. Di Nicola, et al., National ignition facility system alignment, *Appl. Opt.* 50 (8) (2011) 1136–1157.
- [2] A. Casner, T. Caillaud, S. Darbon, et al., LMJ/PETAL laser facility: overview and opportunities for laboratory astrophysics, *High Energy Density Phys.* 17 (2015) 2–11.
- [3] J.L. Miquel, C. Lion, P. Vivini, The Laser Mega-Joule: LMJ & PETAL status and program overview, *J. Phys.: Conf. Ser.* IOP Publishing 688 (1) (2016) 012067.
- [4] R.R. Prasad, M. Bernacil, J. Halpin, J. Peterson, S. Mills, R.P. Hackel, Design of an illumination technique to improve the identification of surface flaws on optics, in: *Proceedings of the XXXVI Boulder Damage Symposium*, International Society for Optics and Photonics, 2005, pp. 421–426.
- [5] D. Liu, S. Wang, P. Cao, L. Li, et al., Dark-field microscopic image stitching method for surface defects evaluation of large fine optics, *Opt. Express* 21 (5) (2013) 5974–5987.
- [6] P. Cao, Y. Yang, C. Li, et al., Alignment methods for micron-scale surface defects automatic evaluation of large-aperture fine optics, *Chin. Opt. Lett.* 307 (4) (2015) 26–30.
- [7] Z. Zhang, X. Tao, D. Xu, et al., Surface flaws detection algorithms for large aperture

- optical element, in: Proceedings of the International Conference on Advanced Mechatronic Systems, Beijing, China, 2015, pp. 485–490.
- [8] X. Tao, Z. Zhang, F. Zhang, D. Xu, A. Novel, A novel and effective surface flaw inspection instrument for large-aperture optical elements, *IEEE Trans. Instrum. Meas.* 64 (9) (2015) 2530–2540.
- [9] D. Liu, Y. Yang, L. Wang, et al., Microscopic scattering imaging measurement and digital evaluation system of defects for fine optical surface, *Opt. Commun.* 278 (2) (2007) 240–246.
- [10] S. Wang, D. Liu, Y. Yang, et al., Distortion correction in surface defects evaluating system of large fine optics, *Opt. Commun.* 312 (2014) 110–116.
- [11] H. Chu, Z. Xie, Q. Liu, Y. Shao, Surface cleanliness inspection apparatus for optical component based on machine vision, in: Proceedings of the 3rd International Congress on Image and Signal Processing, Beijing, China, 2010, pp. 1694–1698.
- [12] L. Yan, Y. Yang, X. Wang, et al., Grayscale adjustment method for CCD mosaic camera in surface defect detection system, in: Proceedings of the 7th International Symposium on Advanced Optical Manufacturing and Testing Technologies (AOMATT 2014), International Society for Optics and Photonics, Harbin, China, 2014, pp. 928235-1–928235-9.
- [13] L. Li, D. Liu, P. Cao, et al., Automated discrimination between digs and dust particles on optical surfaces with dark-field scattering microscopy, *Appl. Opt.* 53 (23) (2014) 5131–5140.
- [14] C. Yang, R. Lu, N. Chen, A fast method for large aperture optical elements surface defects detection, *Adv. Multimed., Softw. Eng. Comput.* (2011) 175–184.
- [15] ISO 10110-7:2008 Optics and Photonics – Preparation of Drawings for Optical Elements and Systems – Part 7: Surface Imperfection Tolerances.
- [16] R.G. von Gioi, J. Jakubowicz, J.M. Morel, et al., LSD: a fast line segment detector with a false detection control, *IEEE Trans. Pattern Anal. Mach. Intell.* 32 (4) (2010) 722–732.
- [17] P. Kultaken, L. Xu, E. Oja, A new curve detection method: randomized Hough transform (RHT), *Pattern Recognit. Lett.* 11 (5) (1990) 331–338.
- [18] A. Torralba, A. Oliva, M. Castelano, J.M. Henderson, Contextual guidance of eye movements and attention in real-world scenes: the role of global features in object search, *Psychol. Rev.* 113 (4) (2006) 766.
- [19] C. Li, Y. Yang, H. Xiong, et al., Dual-threshold algorithm study of weak-scratch extraction based on the filter and difference, *High. Power Laser Part. Beams* 27 (7) (2015) 97–104.
- [20] A. Chondronasios, I. Popov, I. Jordanov, Feature selection for surface defect classification of extruded aluminum profiles, *Int. J. Adv. Manuf. Technol.* 83 (1–4) (2016) 33–41.